

## Research article

Pau Molet, Luz Karimé Gil-Herrera, Juan Luis Garcia-Pomar, Niccolò Caselli, Álvaro Blanco\*, Cefe López and Agustín Mihi\*

# Large area metasurfaces made with spherical silicon resonators

<https://doi.org/10.1515/nanoph-2020-0035>

Received January 16, 2020; revised February 20, 2020; accepted February 22, 2020

**Abstract:** High-index dielectric nanostructures have emerged as an appealing complement to plasmonic nanostructures, offering similar light management capabilities at the nanoscale but free from the inherent optical losses. Despite the great interest in these all-dielectric architectures, their fabrication still requires cumbersome fabrication techniques that limit their implementation in many applications. Hence, the great interest in alternative scalable procedures. Among those, the fabrication of silicon spheres is at the forefront, with several routes available in the literature. However, the exploitation of the Mie modes sustained by these silicon resonators is limited over large areas by polydispersity or a lack of long-range order. Here, we present an all-dielectric metamaterial fabricated with a low cost and highly scalable technique: a combination of soft imprinting nanolithography and chemical vapor deposition. The resulting all-dielectric metasurface is composed of an array of silicon hemispheres on top of a high refractive index dielectric substrate. This architecture allows the exploitation of high-quality Mie resonances at a large scale due to the high monodispersity of the hemispheres organized in a single crystal two-dimensional lattice. The optical response of the metasurface can be engineered by the design parameters

of the nanoimprinted structure. We further demonstrate the potential of this platform to enhance light emission by coupling dye molecules to the sustained Mie resonances and measuring both an eight-fold amplified signal and a triple lifetime reduction.

**Keywords:** all-dielectric metasurface; soft lithography; CVD; large scale photonics; Mie resonance; photoluminescence.

## 1 Introduction

Metallic nanostructures have been intensively studied in recent years due to their capacity to generate a strong light concentration at the sub-wavelength scale, providing new opportunities in photodetection, photocatalysis, photovoltaics, surface-enhanced Raman scattering, photothermal therapy and optical tweezers [1–10]. However, the excitation of plasmonic resonances in metals is inherently associated to optical losses, provoking undesired heating [11, 12] and often, the quenching of light emitters [13], which makes them unappealing for a wide range of applications. The photonics community has also investigated high refractive index nanostructures as alternative means to manage light at the nanoscale in the visible and near infrared (NIR) range with low or no optical losses [14–17]. All-dielectric nanostructures have demonstrated their potential for photo-electrochemical applications [18], light emission [19] and surface-enhanced Raman scattering sensing [20, 21]. Moreover, high-index dielectric nanostructures exhibit resonances with both an electric and a magnetic nature, which can further be exploited in novel photonic phenomena such as magnetic perfect reflection, directional light propagation, electric and magnetic field enhancement, wavefront shaping and Huygens's metasurfaces [22–30].

Among the high-index dielectric materials currently available, silicon has reached a prominence in the field of nanophotonics due to its low cost and straightforward implementation into current complementary metal oxide

**\*Corresponding authors: Álvaro Blanco**, ICMM, Instituto de Ciencia de Materiales de Madrid (ICMM), Consejo Superior de Investigaciones Científicas (CSIC), Sor Juana Inés de la Cruz, 3, 28049 Madrid, Spain, e-mail: a.blanco@csic.es; and **Agustín Mihi**, ICMM, Instituto de Ciencia de Materiales de Barcelona (ICMM-CSIC), Campus UAB, 08193 Bellaterra, Spain, e-mail: amihi@icmm.csic.es. <https://orcid.org/0000-0003-3821-7881>

**Pau Molet and Juan Luis Garcia-Pomar:** ICMM, Instituto de Ciencia de Materiales de Barcelona (ICMM-CSIC), Campus UAB, 08193 Bellaterra, Spain

**Luz Karimé Gil-Herrera, Niccolò Caselli and Cefe López:** ICMM, Instituto de Ciencia de Materiales de Madrid (ICMM), Consejo Superior de Investigaciones Científicas (CSIC), Sor Juana Inés de la Cruz, 3, 28049 Madrid, Spain

semiconductor technologies [31]. In particular, silicon spheres have been widely studied on account of their electric and magnetic dipolar Mie resonances [32]. From a manufacturing perspective, metal spheres benefit from a plethora of solution processing routes that facilitated their exploitation in many disciplines. Silicon colloids, however, are much more difficult to synthesize in solution, hence the energetic pursuit of alternative large area and inexpensive fabrication routes. Silicon spheres have been produced by magnesio-reduction of silicon dioxide colloids [33], chemical vapor deposition (CVD) [34], laser ablation [35] and even grinding macroscopic silicon fragments [36]. However, it remains a challenge to exploit the collective properties of the silicon spheres in large area devices. On the one hand, the polydispersity of the spheres synthesized greatly reduces the quality of the optical response of the ensemble. On the other hand, assembling resonators into complex geometries is not straightforward.

In this work, we demonstrate a large area silicon hemisphere array that serves as a platform to excite electric and magnetic resonances tunable in the wavelength range from 700 nm to 2000 nm. The all-dielectric metasurfaces are fabricated using highly scalable and inexpensive nanopatterning techniques, moving away from classical lithographies involving electron beam lithography and reactive ion etching of wafer source materials, thus bringing these structures closer to applications. The key innovative aspects of this approach are two: firstly, we use a commercial nanocrystalline titania ( $\text{TiO}_2$ ) paste [37, 38] as a nanoimprinting resist to produce temperature-resistant nanostructures; secondly, the silicon is deposited using a low pressure CVD [39] that enables infiltration and coating of the nanostructure. The final metasurface is composed of a two-dimensional array of highly monodisperse silicon hemispheres on a silicon-infiltrated  $\text{TiO}_2$  (Si/ $\text{TiO}_2$ ) waveguide. This inventive architecture is designed to simultaneously sustain Mie resonances from the hemispheres and the quasi-guided modes (QGM) diffracted by the periodic lattice with high Q-factors [40]. Finally, the intense optical response of the metasurface is used to achieve a strong enhancement of the photoluminescence (PL) of NIR light-emitting dye molecules coupled to the resonant modes.

## 2 Unconventional nanofabrication of the metasurface

In order to exploit the Mie resonances exhibited by spherical silicon resonators in a large area metasurface,

it is necessary to use highly uniform resonant units to obtain sharp resonances, useful for photonic applications. Classical lithographies have been used to produce many silicon metasurfaces with high homogeneity and resolution in which many of their exciting properties have been studied, but they still present hurdles in scaling up the process. Most of the silicon colloids fabricated by other methods (CVD, laser ablation, silicon milling, etc.) enabled the study of the Mie resonances on a single particle, but the optical properties are severely affected by the size distribution of the resonators and by their random organization. Herein we have adapted the nanoimprinting lithography (NIL) and CVD techniques for the creation of silicon metasurfaces based in silicon hemispheres. The integration of these techniques allows the generation of a monodisperse array of silicon hemisphere resonators with the desired organization on the substrate surface, combining the resolution, monodispersity and spatial positioning of classical lithographies with a large scale focus for industrial applications.

The fabrication procedure of the metasurface is reduced to two simple steps: the fabrication of a nanostructured mesoporous  $\text{TiO}_2$  (m- $\text{TiO}_2$ ) backbone and the infiltration and coating with silicon (Figure 1). The first step relies on NIL, a technique capable of producing extended nanostructured areas with high fidelity, rapidity, are cleanroom-free and at a low cost [37, 38, 41]. In short, a pre-patterned polydimethylsiloxane mold is pressed against a resist that is left with a negative impression of the pattern (Figure 1A). As an NIL resist, we use a commercially available  $\text{TiO}_2$  nanoparticle paste. The m- $\text{TiO}_2$  paste, once annealed at 545°C, can withstand the 365°C required during the Si-CVD process without cracking or delamination (see Methods); once the organic phase is annealed, a porous network of sintered 20 nm anatase  $\text{TiO}_2$  nanocrystals is left behind. This porosity is later filled with silicon, endowing the structure with a higher refractive index, hence stronger light confinement. It is worth mentioning that a residual layer of resist is left under the pillars after demolding. In our case, we produced 350 nm pillars on a 400 nm thick resist layer (see Figure 1B). The residual layer, once infilled with silicon, will act as a high refractive index waveguide, the thickness of which can be controlled at the spin coating step of the  $\text{TiO}_2$  resist. Next, the silicon coating is deposited via low pressure Si-CVD, following a standard methodology [42]. Amorphous silicon is produced by the decomposition of disilane ( $\text{Si}_2\text{H}_6$ ), which is used as a precursor gas. Silicon growth is essentially governed by two parameters; the precursor gas pressure and the temperature of decomposition. Since in our set up the decomposition of disilane

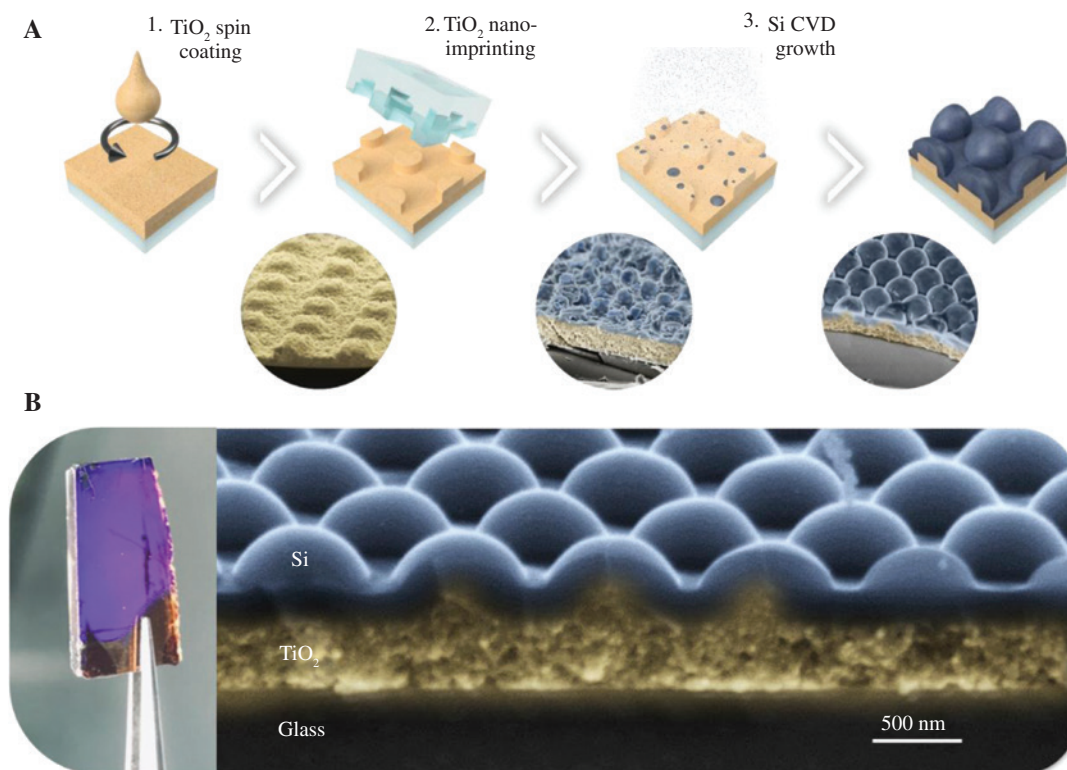


**Figure 1:** Si metasurface fabrication.

(A) Schematics of the different steps involved, namely: (1) spin casting the titania paste, (2) nanoimprinting and annealing step and (3) silicon coating by chemical vapor deposition (CVD). (B) Scanning electron microscopy (SEM) cross section and photograph of a fabricated sample.

is allowed to proceed to termination, it is the gas pressure that determines the amount of infiltrated silicon for a fixed temperature [34]. The choice of temperature regulates the decomposition rate of disilane into silicon (see Methods) [43]. Initially, the silicon infiltrates the m-TiO<sub>2</sub> backbone, increasing the refractive index of the structure. Once the porosity of the m-TiO<sub>2</sub> is filled, the CVD conformal growth reaches a phase of accumulation of material on the top of the imprinted m-TiO<sub>2</sub> pillars, leading to the formation of the silicon-hemispheres (Figure 1B). The resulting hemispheres present a low polydispersity with standard deviations below 2% (Supporting Figure S1), improving the monodispersity values from previous large scale fabrication reports [36, 44]. Furthermore, the hemispheres are assembled into a single crystal array covering areas as large as 1 cm<sup>2</sup>. The metasurface displays strong iridescence and rich reflection and transmission spectra in which the presence of sharp resonances can be clearly distinguished and correlated with the finite-difference time-domain (FDTD) simulated response of the structure (Figure 2A, in which we investigated a structure with a lattice parameter of  $L=600$  nm).

Due to the high refractive index of the semiconductor, the different components of the metasurface

influence its overall optical response, as illustrated by the spatial distribution of the electromagnetic fields calculated by FDTD (Figure 2). The silicon hemispheres organized in a two-dimensional lattice act as Mie resonators and diffraction scatterers, while the residual layer behaves as a high refractive index waveguide capable of supporting QGM (Supporting Figures S2 and S3). These QGM or leaky modes are modes with attenuation due to the radiation towards external surroundings. Similarly to a grating coupler on top of a waveguide, the array of hemispheres grants extra momentum to the radiative modes to couple to guided modes. However, by the same phenomena, these modes are leaky and can out-couple to radiative modes such as the Mie modes of the hemispheres. The intercoupling between the electric and magnetic dipolar Mie resonances (ED and MD) and the QGM are inferred by field distribution along the structure (Figure 2B, E). The electric and magnetic fields calculated inside the structure confirm the presence of transversal electric (TE) and transversal magnetic (TM) QGM hybridized with the ED and MD of the Mie resonances of the hemisphere. The electric modes ED-TE0 and the ED-TE1 appear as sharp resonances at 1309 nm and 1139 nm wavelengths, respectively, and present a strong



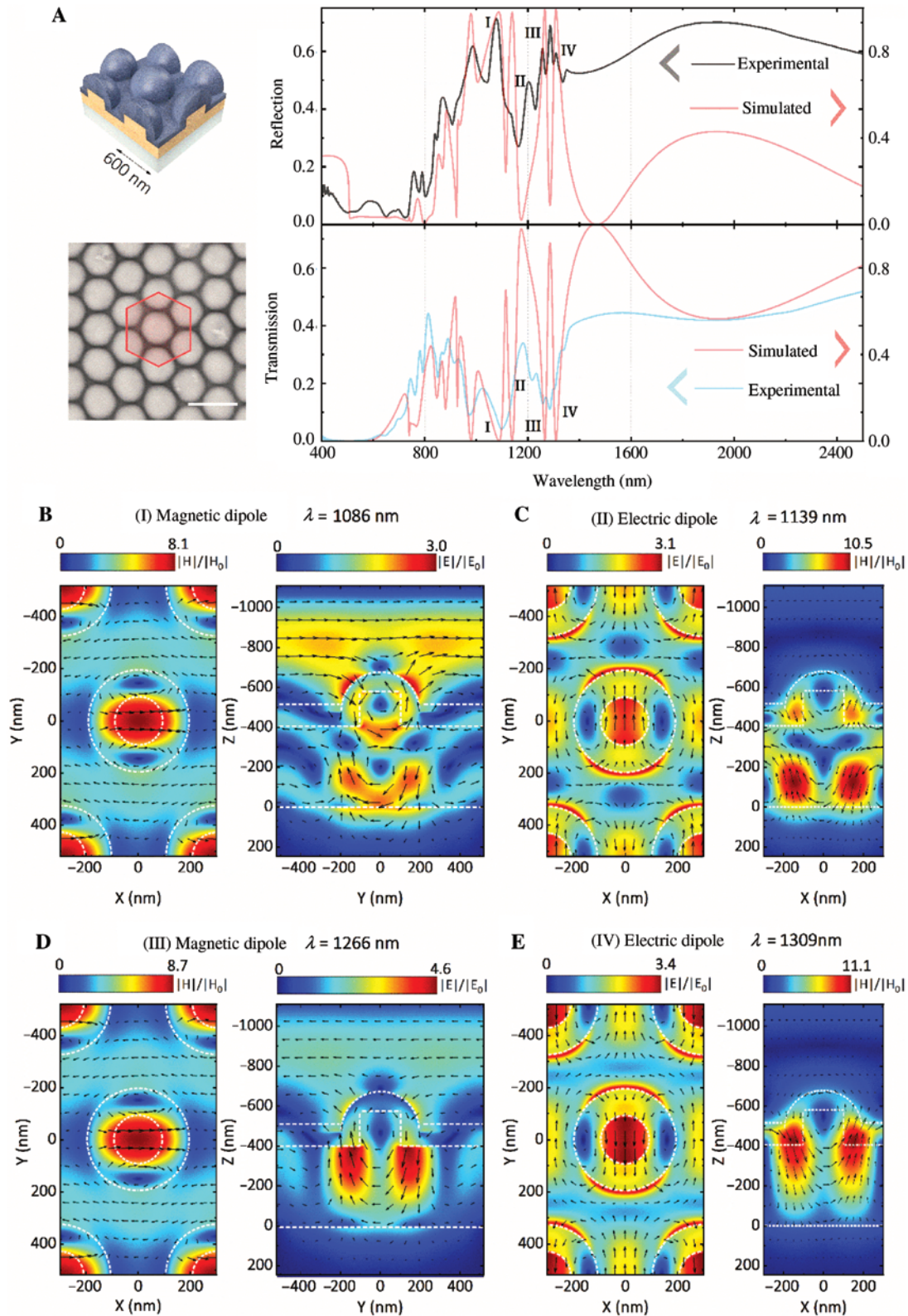


**Figure 2:** Optical response of the metasurface with lattice parameter  $L = 600$  nm on a 400 nm Si/TiO<sub>2</sub> waveguide.

(A) Experimental vs. simulated reflectance and transmittance. Insets: schematics of the metasurface and scanning electron microscopy (SEM) top view (scale bar = 1  $\mu$ m). Spatial distribution and nature of the electromagnetic fields for the different resonances highlighted in I-IV; namely (B)  $\lambda = 1086$  nm (MD-TM1), (C)  $\lambda = 1139$  nm (ED-TE1), (D)  $\lambda = 1266$  nm (MD-TM0) and (E)  $\lambda = 1309$  nm (ED-TE0). See Methods for details on the finite-difference time-domain (FDTD) simulations.

circulation of the magnetic fields in the hemisphere, thus conferring an intense electrical dipolar moment to the particle (Figure 2C and E). We observe the same trend in the MD-TM<sub>0</sub> and MD-TM<sub>1</sub> modes placed at 1266 nm and 1086 nm, which present a strong MD in the hemisphere caused by the circulation of the electric field (Figure 2B and D). The MD-TM and ED-TE nature of the resonances is further confirmed by the angular dependence of these resonances and multipolar decomposition (depicted in Supporting Figures S4 and S5). The presence of strong dipolar moments proves that we have developed a platform capable of exploiting Mie resonances at a large scale, since the different resonances are identified even when illuminating large areas (reflectance and transmission measurements were performed through a  $4\times$  objective and 0.1 NA, see Methods) on account of the high homogeneity achieved. A thorough study of the origin of the optical response of a metasurface with lattice parameter  $L = 300$  nm is shown in Supporting Figures S6–S8.

The seamless fabrication technique allows engineering of the electromagnetic resonances targeting desired regions of the spectrum solely by changing the lattice parameter of the nanoimprinted structure. This tunability is illustrated in Figure 3, where cross sectional

scanning electron microscopy (SEM) and experimental reflectance and transmittance are shown for samples with increasing lattice parameter. Furthermore, this metasurface offers new possibilities for inverting the spectral position of the ED with respect to the MD (Supporting Figure S9) as has been seen in previous work for squared lattices [22, 45, 46]. The versatility of the technique also allowed us to explore other hemisphere sizes and geometries, such as squared lattices, which behaved similarly (Supporting Figures S10 and S11). Moreover, the geometrical parameters of the structure can be adjusted seeking the overlap of the magnetic and electric modes that induces a first Kerker effect, a long sought condition to suppress backward scattering in the structure [47, 48].

### 3 Enhancing PL with all-dielectric metasurfaces

Finally, we tested the ability of our metasurface to enhance the PL of light emitters deposited on top of the structure (Figure 4A), as a proof of principle to illustrate their photonic applications. We selected the IR-140 dye [49] that exhibits an emission band from 750 nm to 900 nm and can be readily deposited by spin coating on the metasurface. To maximize the interaction of the studied resonances with the dye, we chose the metasurface with  $L = 300$  nm since the dipolar-QGM reflection peaks of this structure (Figure 4B) match well the emission of the dye. The dipolar quasi-guided resonances accumulate density of states in the substrate surface responsible for the modification of the emission rate of the dye (Supporting Figure S12). As a consequence, the PL spectra of the dye deposited on the metasurface are greatly reinforced with various peaks clearly distinguishable (Figure 4B). These peaks closely match the positions of the optical resonances of the metasurface, as illustrated by comparing the PL signal with reflection measurements. The PL from a flat sample with equivalent dielectric contrast is also presented for comparison, giving an eight-fold PL enhancement. This finding illustrates the great potential of the metasurface modes to be coupled to light emitters. Moreover, to further characterize the interaction, we evaluated how the increased density of electromagnetic states in the near-field of the metasurface increases the decay rate, reducing the PL lifetime (Purcell effect). In particular, we measured and compared the time-resolved PL of emitters deposited on the sample and on the reference plane (Figure 4C). The former shows a faster decay, a shortened PL lifetime, which indicates a

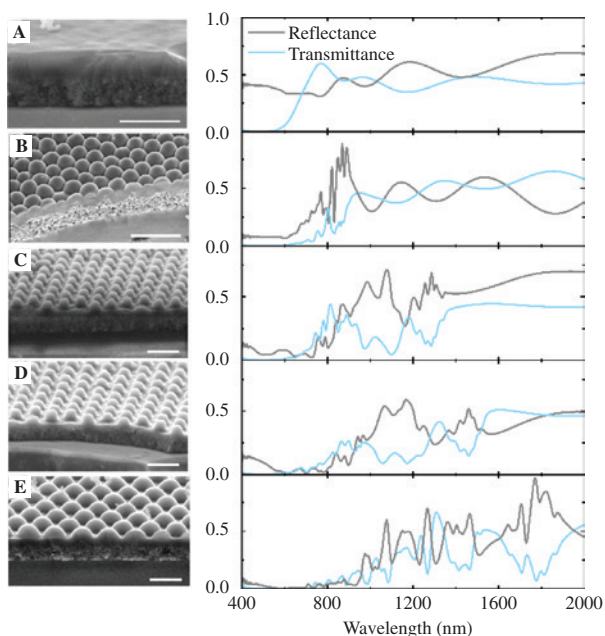


**Figure 3:** Optical response of all-dielectric metasurfaces with varying lattice parameters.

Scanning electron microscopy (SEM) inclined view and optical reflectance (black) vs. transmittance (blue) spectra of (A) flat reference sample and (B) hexagonal metasurfaces with lattice parameters of 300 nm, (C) 600 nm, (D) 700 nm and (E) 800 nm. (Scale bar = 1  $\mu$ m).

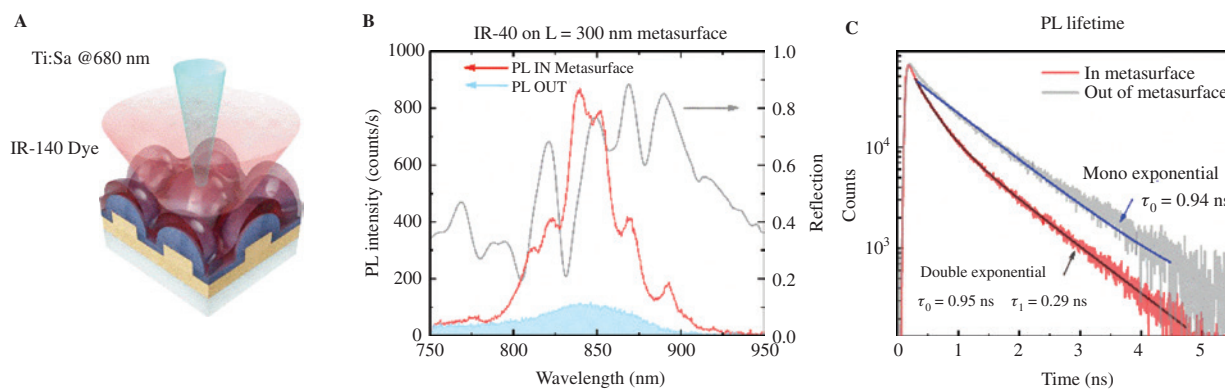


**Figure 4:** Photoluminescence (PL) enhancement of a near infrared (NIR) dye on the metasurface.

(A) Scheme of PL measurement configuration. The emission of the spin coated dye on the metasurface ( $L=300$  nm) is excited by a Ti:sapphire laser and collected in reflectance mode by a 5 cm lens. (B) PL intensity of the dye placed on the metasurface (red) vs. on a planar silicon substrate (blue); the reflection of the nanostructured substrate (gray) is included for comparison. (C) Spectrally integrated time-resolved PL decay for emitters deposited on the metasurface (red) and on the reference substrate (grey) with their corresponding fitting curves.

more efficient PL response with an enhanced spontaneous emission rate. In particular, the time-resolved emission of the dye on the planar sample follows a mono-exponential decay (with  $\tau=0.94$  ns), while a double exponential decay is found when the dye is placed on the metasurface (with  $\tau_0=0.95$  ns and  $\tau_1=0.29$  ns). Interestingly, the slow component of the double exponential decay ( $\tau_0$ ) is consistent with the intrinsic lifetime of the dye on the reference plane, indicating that it originates from the molecules that do not interact with the Mie-QGM resonances. Finally, we evaluate the Purcell factor ( $P$ ) of the spontaneous emission rate as  $P=\tau_1^{-1}-\tau_0^{-1}=2.4$  by using the relationship found in previous reports [50].

## 4 Conclusions

In this work, we present an all-dielectric metasurface designed to exploit strong Mie type resonances in large areas that can be fabricated with a low cost and by highly scalable techniques such as NIL and low pressure CVD. The highly homogeneous silicon hemispheres fabricated are arranged on top of a high refractive index substrate and exhibit sharp hybridized Mie-QGM with both electric and magnetic natures. These modes endow the metasurface with intense field enhancements, having potential in many photonic applications, as we demonstrate by an enhanced PL from an NIR dye placed atop. We also provide key guidelines to optimize the substrate efficiency and response for different applications by varying its geometrical parameters with an easy tuning of the fabrication conditions.

## 5 Experimental section

### 5.1 Metasurface fabrication

#### 5.1.1 TiO<sub>2</sub> backbone fabrication

A 300 nm layer of 90 T [Dyesol (greatcellsolar), Elanora, Australia] transparent TiO<sub>2</sub> paste composed of 20 nm anatase TiO<sub>2</sub> nanoparticles was spin coated on the glass substrates. The initial paste was diluted at 1:3 (w/w) in ethanol and spin coated at 2000 rpm with 1000 rpm/s acceleration for 10 s. The nanoimprinting procedure took place after the layer deposition, pressing the 1 cm<sup>2</sup> pre-patterned polydimethylsiloxane (PDMS, Sylgard 184 Dow, Midland, MI, USA) stamp onto the sample on a hotplate at 125°C for 10 min. Once the paste was imprinted, a hard bake treatment to 545°C during 1 h was done.

#### 5.1.2 Silicon infiltration

Silicon deposition was achieved by low pressure, low temperature CVD using S<sub>2</sub>H<sub>6</sub> gas as a precursor. Porous TiO<sub>2</sub> structures were placed in an ampoule under vacuum (10<sup>-6</sup> Torr) where disilane at the desired pressure was condensed and then decomposed at 365°C for 1 h. The amount of infiltrated silicon was controlled by adjusting the chamber pressure between 70 Torr and 110 Torr. After silicon infiltration, the Si/TiO<sub>2</sub> was cleaned gently with acetone to remove any byproduct that could have been deposited on the surface.



### 5.1.3 Dye deposition

The dye IR-140 (Sigma Aldrich, St. Louis, MO, USA) emits in the spectral range of 750–900 nm. The dye was dispersed to a 0.35 wt% concentration in a biopolymer film made of a deoxyribonucleic acid (DNA)-cetyltrimethylammonium polymer matrix salmon DNA (by Sigma Aldrich) [51]. The DNA matrix has been chosen due to the low quenching contribution to the dye efficiency. The optically active matrix was deposited by spin coating 2  $\mu$ l of an ethanol solution of DNA and dye at 6000 rpm for 1 min, giving rise to a film of a few  $\mu$ m thickness. The same procedure was applied on both the metasurface and the reference silicon planar surface.

## 5.2 FDTD modeling

The numerical simulations were performed using commercial FDTD software (www.lumerical.com, Vancouver, BC, Canada) and verified with the Wave Optics module of COMSOL Multiphysics (www.comsol.com, Stockholm, Sweden). The calculations reproduced the schematics shown in Figure 2 with the geometrical parameters extracted from SEM micrographs of the fabricated samples. A linearly polarized plane wave source impinging a unit cell was modeled providing a good agreement with the experimental results. Refractive indexes of the amorphous silicon [52] and  $\text{TiO}_2$  [53] were extracted from literature. The refractive index of the m- $\text{TiO}_2$  embedded with silicon was obtained by a three-component composite material effective medium approximation considering amorphous silicon,  $\text{TiO}_2$  and air [54].

## 5.3 Far-field reflection measurements

A Fourier transform infrared spectrophotometer attached to an optical microscope (Vertex 70 and Hyperion, Bruker, Billerica, MA, USA) was used to obtain the far-field reflection measurements in the 400–2200 nm range. The background reflection spectrum was set with a silver mirror which exhibits a 96% reflectivity in the tested range of wavelengths. Reflected light was collected through a 4 $\times$  objective with a 0.10 numerical aperture and a 2 $\times$ 2 mm<sup>2</sup> spatial aperture.

## 5.4 SEM

SEM images were obtained by two scanning electron microscopes: QUANTA FEI 200 FEG-ESEM with a field emission gun source and LEO 145 FESEM (Hitachi S-4700).

All the images were taken using 5 kV and 2 kV beams, respectively, to generate the secondary electrons in a high vacuum regime ( $10^{-3}$  Pa).

## 5.5 PL measurements

The PL is excited by focusing a Ti:sapphire laser (Chameleon model by Coherent, Santa Clara, CA, USA; 1 kHz repetition rate, 150 fs pulse width, the emission of which is bandpass filtered around 680 nm) through a 5 cm focal length lens. The average power impinging on the sample is 500  $\mu$ W. The dye emission is collected by the same lens in illumination/collection geometry. After filtering the laser contribution, the PL is coupled into an optical fiber and alternatively connected to i) a compact spectrometer (USB 2000, Ocean Optics, Edinburgh, UK; 0.3 nm resolution) to obtain the spectral information or ii) to an avalanche photodiode to perform time-correlated single photon counting by using an integrated electronic module (by Becker & Hickl) in order to get the time-resolved PL decay in the ns time range.

# 6 Supporting information

Supporting Information is available from the Wiley Online Library or from the author.

**Acknowledgements:** We greatly acknowledge financial support from the Spanish Ministry of Science, Innovation and Universities with projects MAT2016-79053-P and RTI2018-093921-B-C41 and the excellence program SEV-2015-0496; Generalitat de Catalunya program AGAUR 2017-SGR-00488; and the European Research Council under the European Union's Horizon 2020 research and innovation program (grant number 637116, Funder Id: <http://dx.doi.org/10.13039/100010663>). P.M. acknowledges financial support from an FPI contract (2017) of the MICINN (Spain) cofounded by the ESF and UAB school doctoral program. L.K.G. acknowledges a COLCIENCIAS doctoral grant. N.C. acknowledges the JdIC programme.

**Conflict of interest:** The authors declare no conflict of interest.

# References

- [1] Huang X, Jain PK, El-Sayed IH, El-Sayed MA. Plasmonic photothermal therapy (PPTT) using gold nanoparticles. *Lasers Med Sci* 2008;23:217–28.

- [2] Atwater HA, Polman A. Plasmonics for improved photovoltaic devices. *Nat Mater* 2010;9:205–13.
- [3] Ferry VE, Verschuuren MA, Li HBT, et al. Light trapping in ultrathin plasmonic solar cells. *Opt Express* 2010;18:A237.
- [4] Liu Y, Cheng R, Liao L, et al. Plasmon resonance enhanced multicolour photodetection by graphene. *Nat Commun* 2011;2:1.
- [5] Wang P, Huang B, Dai Y, Whangbo M-H. Plasmonic photocatalysts: harvesting visible light with noble metal nanoparticles. *Phys Chem Chem Phys* 2012;14:9813.
- [6] Brongersma ML, Halas NJ, Nordlander P. Plasmon-induced hot carrier science and technology. *Nat Nanotechnol* 2015;10:25–34.
- [7] Matricardi C, Hanske C, Garcia-Pomar JL, Langer J, Mihi A, Liz-Marzán LM. Gold Nanoparticle plasmonic superlattices as surface-enhanced raman spectroscopy substrates. *ACS Nano* 2018;12:8531–9.
- [8] Espinha A, Dore C, Matricardi C, Alonso MI, Goñi AR, Mihi A. Hydroxypropyl cellulose photonic architectures by soft nanoimprinting lithography. *Nat Photonics* 2018;12:343–8.
- [9] Chanda D, Shigeta K, Truong T, et al. Coupling of plasmonic and optical cavity modes in quasi-three-dimensional plasmonic crystals. *Nat Commun* 2011;2:479.
- [10] Baek S, Molet P, Choi M, et al. Nanostructured back reflectors for efficient colloidal quantum-dot infrared optoelectronics. *Adv Mater* 2019;31:1901745.
- [11] Zolotavin P, Alabastri A, Nordlander P, Natelson D. Plasmonic heating in Au nanowires at low temperatures: the role of thermal boundary resistance. *ACS Nano* 2016;10:6972–9.
- [12] Ammari H, Romero F, Ruiz M. Heat generation with plasmonic nanoparticles. *Soc Ind Appl Math* 2017;16:356–84.
- [13] Faggiani R, Yang J, Lalanne P. Quenching, plasmonic, and radiative decays in nanogap emitting devices. *ACS Photonics* 2015;2:1739–44.
- [14] Mie G. Beiträge zur Optik trüber Medien, speziell kolloidaler Metallösungen. *Ann Phys* 1908;330:377–445.
- [15] Kuznetsov AI, Miroshnichenko AE, Fu YH, Zhang J, Luk'yanchuk B. Magnetic light. *Sci Rep* 2012;2:492.
- [16] van de Groep J, Polman A. Designing dielectric resonators on substrates: combining magnetic and electric resonances. *Opt Express* 2013;21:26285.
- [17] Luk'yanchuk B, Paniagua-Domínguez R, Kuznetsov AI, Miroshnichenko AE, Kivshar YS. Suppression of scattering for small dielectric particles: Anapole mode and invisibility. *Philos Trans R Soc A* 2017;375:20160069.
- [18] Ghobadi A, Ulusoy Ghobadi TG, Karadas F, Ozbay E. Semiconductor thin film based metasurfaces and metamaterials for photovoltaic and photoelectrochemical water splitting applications. *Adv Opt Mater* 2019;7:1900028.
- [19] Krasnok AE, Miroshnichenko AE, Belov PA, Kivshar YS. All-dielectric optical nanoantennas. *Opt Express* 2012;20:20599.
- [20] Rodríguez I, Shi L, Lu X, Korgel BA, Alvarez-Puebla RA, Meseguer F. Silicon nanoparticles as Raman scattering enhancers. *Nanoscale* 2014;6:5666–70.
- [21] Alessandri I, Lombardi JR. Enhanced Raman scattering with dielectrics. *Chem Rev* 2016;116:14921–81.
- [22] Babicheva VE, Moloney JV. Lattice effect on electric and magnetic resonance overlap in periodic array. *Nanophotonics* 2018;7:1663–68.
- [23] Leung S-F, Gu L, Zhang Q, et al. Roll-to-roll fabrication of large scale and regular arrays of three-dimensional nano-spikes for high efficiency and flexible photovoltaics. *Sci Rep* 2014;4:094507.
- [24] Wood T, Naffouti M, Berthelot J, et al. All-dielectric color filters using SiGe-based Mie resonator arrays. *ACS Photonics* 2017;4:873–83.
- [25] Bakker RM, Permyakov D, Yu YF, et al. Magnetic and electric hotspots with silicon nanodimers. *Nano Lett* 2015;15:2137–42.
- [26] Epstein A, Eleftheriades GV. Huygens' metasurfaces via the equivalence principle: design and applications. *J Opt Soc Am B* 2016;33:A31.
- [27] Molet P, Garcia-Pomar JL, Matricardi C, Garriga M, Alonso MI, Mihi A. Ultrathin semiconductor superabsorbers from the visible to the near-infrared. *Adv Mater* 2018;30:1705876.
- [28] Paniagua-Domínguez R, Yu YF, Khaidarov E, et al. A metalens with a near-unity numerical aperture. *Nano Lett* 2018;18:2124–32.
- [29] Komar A, Paniagua-Domínguez R, Miroshnichenko A, et al. Dynamic beam switching by liquid crystal tunable dielectric metasurfaces. *ACS Photonics* 2018;5:1742–8.
- [30] Solomon ML, Hu J, Lawrence M, García-Etxarri A, Dionne JA. Enantiospecific optical enhancement of chiral sensing and separation with dielectric metasurfaces. *ACS Photonics* 2019;6:43–9.
- [31] Staude I, Schilling J. Metamaterial-inspired silicon nanophotonics. *Nat Photonics* 2017;11:274–84.
- [32] García-Etxarri A, Gómez-Medina R, Froufe-Pérez LS, et al. Strong magnetic response of submicron silicon particles in the infrared. *Opt Express* 2011;19:4815.
- [33] Ibisate M, Golmayo D, López C. Silicon direct opals. *Adv Mater* 2009;21:2899–902.
- [34] Fenollosa R, Garín M, Meseguer F. Spherical silicon photonic microcavities: From amorphous to polycrystalline. *Phys Rev B* 2016;93:235307.
- [35] Fu YH, Kuznetsov AI, Miroshnichenko AE, Yu YF, Luk'yanchuk B. Directional visible light scattering by silicon nanoparticles. *Nat Commun* 2013;4:1527.
- [36] Chaâbani W, Proust J, Movsesyan A, et al. Large-scale and low-cost fabrication of silicon mie resonators. *ACS Nano* 2019;13:4199–208.
- [37] Xia Y, Whitesides GM. Soft Lithography. *Angew Chem Int Ed Engl* 1998;37:550–75.
- [38] Xia Y, Rogers JA, Paul KE, Whitesides GM. Unconventional methods for fabricating and patterning nanostructures. *Chem Rev* 1999;99:1823–48.
- [39] Joseph M, Jasinski SMG. Silicon chemical vapor deposition one step at a time: fundamental studies of silicon hydride chemistry. *Acc Chem Res* 1991;24:9–15.
- [40] Alberucci A, Marrucci L, Assanto G. Light confinement via periodic modulation of the refractive index. *New J Phys* 2013;15:083013.
- [41] Qin D, Xia Y, Whitesides GM. Soft lithography for micro- and nanoscale patterning. *Nat Protoc* 2010;5:491–502.
- [42] Blanco A, Chomski E, Grubbschak S, et al. Large-scale synthesis of a silicon photonic crystal with a complete three-dimensional bandgap near 1.5 micrometres. *Nature* 2000;405:437–40.
- [43] García-Santamaría F, Ibisate M, Rodríguez I, Meseguer F, López C. Photonic band engineering in opals by growth of Si/Ge multilayer shells. *Adv Mater* 2003;15:788–92.
- [44] Li X, Pyatenko A, Shimizu Y, Wang H, Koga K, Koshizaki N. Fabrication of crystalline silicon spheres by selective laser heating in liquid medium. *Langmuir* 2011;27:5076–80.



- [45] Campione S, Basilio LI, Warne LK, Sinclair MB. Tailoring dielectric resonator geometries for directional scattering and Huygens' metasurfaces. *Opt Express* 2015;23:2293.
  - [46] Babicheva VE, Evlyukhin AB. Resonant lattice kerker effect in metasurfaces with electric and magnetic optical responses. *Laser Photonics Rev* 2017;11:1700132.
  - [47] Algorri JF, García-Cámara B, Cuadrado A, Sánchez-Pena JM, Vergaz R. Selective dielectric metasurfaces based on directional conditions of silicon nanopillars. *Nanomaterials* 2017;7:177.
  - [48] Yu YF, Zhu AY, Paniagua-Domínguez R, Fu YH, Luk'yanchuk B, Kuznetsov AI. High-transmission dielectric metasurface with  $2\pi$  phase control at visible wavelengths. *Laser Photonics Rev* 2015;9:412–8.
  - [49] Wang D, Jiang H, Yang H, et al. Investigation on photoexcited dynamics of IR-140 dye in ethanol by femtosecond supercontinuum-probing technique. *J Opt A: Pure Appl Opt* 2002;4:155–9.
  - [50] Zhou W, Dridi M, Suh J Y, et al. Lasing action in strongly coupled plasmonic nanocavity arrays. *Nat Nanotechnol* 2013;8:506–11.
  - [51] Yu Z, Li W, Hagen J A, et al. Photoluminescence and lasing from deoxyribonucleic acid (DNA) thin films doped with sulforhodamine. *Appl Opt* 2007;46:1507.
  - [52] Gomard G, Drouard E, Letartre X, et al. Two-dimensional photonic crystal for absorption enhancement in hydrogenated amorphous silicon thin film solar cells. *J Appl Phys* 2010;108:123102.
  - [53] DeVore J R. Refractive indices of rutile and sphalerite. *J Opt Soc Am* 1951;41:416.
  - [54] Luo R. Effective medium theories for the optical properties of three-component composite materials. *Appl Opt* 1997;36:8153–8.
- 
- Supplementary Material:** The online version of this article offers supplementary material (<https://doi.org/10.1515/nanoph-2020-0035>).